The super greenhouse effect in a changing climate

The Super Greenhouse Effect in a Changing Climate

GRAEME L. STEPHENS

Jet Propulsion Laboratory, California Institute of Technology, Pasadena, California, and Department of Meteorology, University of Reading, Reading, United Kingdom

BRIAN H. KAHN AND MARK RICHARDSON

Jet Propulsion Laboratory, California Institute of Technology, Pasadena, California

(Manuscript received 30 March 2015, in final form 2 April 2016)

ABSTRACT

In all outputs of the 1% yr^{-1} increase in CO_2 climate model experiments archived under the World Climate Research Programme's (WCRP) phase 5 of the Coupled Model Intercomparison Project (CMIP5), regions exist in the low latitudes where both the clear-sky and all-sky OLR decrease with surface warming. These are identified as regions of positive longwave feedback and are regions of a super greenhouse effect (SGE). These SGE regions are identified from feedback analysis of the $4 \times CO_2$ abrupt experiments of CMIP5, and despite their existence, there is little agreement across models as to the magnitude of the effect. The general effects of clouds on the SGE are to amplify the clear-sky SGE, but there is also poor agreement on the magnitude of the amplification that varies by an order of magnitude across models. Sensitivity analyses indicate that localized SGE regions are spatially aligned with a large moistening of the upper troposphere. The reduction in clear-sky OLR arises from a reduction in emission in the far IR with nonnegligible contributions from mid-IR emission from the midtroposphere. When viewed in the broader context of meridional heat transport, it is found that of the 1.03-PW rate of heat gained globally, 0.8 PW is absorbed in the tropics and is contributed almost equally by reductions in clear-sky longwave emission (i.e., the clear-sky SGE) and increased absorbed clear-sky solar radiation associated with increased water vapor. The processes that define the clear-sky SGE are shown to be fundamental to the way models accumulate heat and then transport it poleward.

1. Introduction

The fundamental importance of the earth's greenhouse effect to the earth's climate has been appreciated for some time. Fourier (1824) first proposed its existence and Tyndall (1861) made the first quantitative measurements of the strength of greenhouse absorbers in the laboratory. Arrhenius (1896), influenced by the works of Fourier and Tyndall, produced the first calculations of how changes to the levels of carbon dioxide in the atmosphere alter the surface temperature through changes in the greenhouse effect.

Perhaps one of the most important consequences of the existence of a greenhouse effect on our climate is the positive feedback that it produces as a result of the connections between temperature, water vapor, and emission of infrared radiation. This feedback acts upon an increase in carbon dioxide that induces a warming, a consequent increase in water vapor, and a strengthened greenhouse effect that further warms the climate (e.g., Held and Soden 2000). Although the magnitude of this positive feedback has been a topic of discussion for some time, mostly regarding the role of changes to tiny amounts of water vapor high in the troposphere (Soden et al. 2005; Dessler and Davis 2010) or stratosphere (Solomon et al. 2010; Dessler et al. 2013), there is now ample evidence that suggests the feedback is positive throughout most layers of the earth's lower atmosphere by way of connections between temperature and water vapor (Soden and Held 2006) as well as longwave flux emitted to the surface (Stephens and Hu 2010). Modeling and observational studies have attributed a majority of the moistening in both the total column water vapor (Santer et al. 2007) and upper-tropospheric water vapor (Chung et al. 2014) to anthropogenic climate change.

Corresponding author address: Graeme Stephens, Jet Propulsion Laboratory, 4800 Oak Grove Dr., Mail Stop 233-304, Pasadena, CA 91109.
E-mail: graeme.stephens@jpl.nasa.gov

DOI: 10.1175/JCLI-D-15-0234.1

The term "super greenhouse" has been used in a number of contexts. Super greenhouse gas was coined to refer to those gases like hydrofluorocarbons (IPCC 2013) that are deemed to be disproportionately strong absorbers of infrared radiation on a molecule-by-molecule basis compared to, for instance, carbon dioxide (e.g., Hong et al. 2013). The term super greenhouse climate is used in a paleoclimate context to describe periods of great warmth like the Cretaceous Thermal Maximum about 90 million years ago when it is estimated that the surface temperatures of tropical oceans reached 35°C and sea levels elevated, all coinciding with a more extreme carbon cycle with much higher levels of carbon dioxide in the atmosphere than today (Bornemann et al. 2008). The super greenhouse effect (SGE) has also been used to describe a particular characteristic of the greenhouse effect mostly in tropical regions (Raval and Ramanathan 1989; Valero et al. 1997; Hallberg and Inamdar 1993) based on the observed relation between spatiotemporal patterns of longwave fluxes and sea surface temperatures. In this context, the SGE refers to those regions where the emission to the surface [the downward longwave radiation (DLR)] increases with increasing SSTs at a rate that exceeds changes to the outgoing longwave radiation emitted to space (OLR) as SSTs increase (e.g., Stephens and Greenwald 1991). Valero et al. (1997) introduce the SGE in terms of the following measure of the earth's greenhouse G:

$$G = \varepsilon\sigma(\mathrm{SST})^4 - \mathrm{OLR}, \tag{1}$$

where SST is the sea surface temperature, σ is the Stefan–Boltzmann constant, and ε is the emissivity of the sea surface. According to this definition, the SGE is present in those regions where the increase in G with SST exceeds the increase in surface emission $\varepsilon\sigma\mathrm{SST}^4$:

$$\mathrm{SGE} = \frac{dG}{d\mathrm{SST}} > 4\varepsilon\sigma\mathrm{SST}^3. \tag{2}$$

It follows from (1) and (2) that this occurs when

$$\frac{d\mathrm{OLR}}{d\mathrm{SST}} < 0. \tag{3}$$

Using spatial patterns of SST and OLR, Valero et al. (1997) find that about 50% of the tropical region between latitudes 20°N and 20°S is subject to the SGE.

While past studies infer (3) from spatiotemporal changes in SST using natural modes of variability such as ENSO, the SGE of this study is introduced here in a slightly different way. The SGE is not simply defined by an SST threshold as in Hallberg and Inamdar (1993) or from gradients of SST as in Valero et al. (1997), but rather it is derived from changes in the OLR that result in response to a surface warming induced by increased greenhouse gases. The model experiments used to analyze this SGE are described in the next section, and the SGE is defined from the feedback analysis of the $4 \times CO_2$ abrupt experiments archived under the World Climate Research Programme's (WCRP) phase 5 of the Coupled Model Intercomparison Project (CMIP5) (Taylor et al. 2012). The results of this feedback analysis are described in section 3 and followed in section 4 by a discussion of the feedback factors that shape the changes in OLR observed in the $1\%\,\mathrm{yr}^{-1}$ increase in CO_2 transient experiments. Sensitivity analyses outlined in section 5 are used to point to the processes responsible for the clear-sky component of the SGE. Since the SGE is a property of climate change, the implications of the SGE to climate change projected by climate models are discussed in section 6.

2. Model data and the SGE

The SGE is an important consequence of feedbacks that occur as the earth warms. The SGE is defined here using the forcing–response analysis introduced by Gregory et al. (2004) as implemented regionally by Andrews et al. (2015). This framework is underpinned by a simple linear relation between global radiative forcing F ($\mathrm{W\,m^{-2}}$), the change in net TOA radiative flux ΔN ($\mathrm{W\,m^{-2}}$), and surface temperature change ΔT (K):

$$\Delta N = F + \alpha\Delta T, \tag{4}$$

where α is a measure of all climate feedbacks. This linear analysis assumes these feedbacks are constant over time and is estimated from model experiments in which F is held constant, such as occurs in the abrupt $4 \times CO_2$ climate model experiments. This linear analysis can also be applied to each of the additive components of the net flux change, thereby determining the feedback strengths of the processes that shape these respective components. For example, analysis of clear-sky OLR provides a joint measure of Planck and water vapor longwave (LW) feedbacks, and analysis of the clear-sky solar absorption includes combinations of surface albedo and water vapor feedbacks (e.g., Andrews and Ringer 2014). In this study, as in Andrews et al. (2015), we regress changes in local TOA fluxes onto global mean ΔT to obtain local values of α. The SGE then follows as those regions where

$$\alpha_{\mathrm{OLR}} > 0, \tag{5}$$

which is analogous to the definition of (3) but now the SGE is defined with respect to measures of positive feedbacks on the OLR.

TABLE 1. Atmosphere–ocean coupled CMIP5 models analyzed in this study. The modeling centers are identified as contributors to the 1% yr^{-1} transient experiment (14 contributors), abrupt $4 \times CO_2$ experiment (26 contributors), or both experiments. (Acronym expansions are available online at http://www.ametsoc.org/PubsAcronymList.)

Modeling center	Acronym	Model name	Experiment
Beijing Climate Center, China	BCC	BCC_CSM1.1	Abrupt and transient
College of Global Change and Earth System Science, Beijing Normal University, China	GCESS	BNU-ESM	Abrupt
Canadian Centre for Climate Modelling and Analysis, Canada	CCCma	CanESM2	Abrupt and transient
Centre National de Recherches Météorologiques—Groupe d'études de l'Atmosphère Météorologique (CNRM-GAME) and Centre Européen de Recherche et de Formation Avancée en Calcul Scientifique (CERFACS), France	CNRM	CNRM-CM5	Abrupt
CNRM-GAME and CERFACS, France	CNRM	CNRM-CM5.2	Abrupt
Commonwealth Scientific and Industrial Research Organisation (CSIRO)/Queensland Climate Change Centre of Excellence, Australia	CSIRO-QCCCE	CSIRO Mk3.6.0	Abrupt and transient
CSIRO and Bureau of Meteorology (BoM), Australia	CSIRO-BOM	ACCESS1.0	Abrupt
CSIRO and BoM, Australia	CSIRO-BOM	ACCESS1.3	Abrupt
State Key Laboratory of Numerical Modeling for Atmospheric Sciences and Geophysical Fluid Dynamics (LASG) at the Institute of Atmospheric Physics (IAP), and Center for Earth System Science (CESS), Tsinghua University, China	FGOALS	FGOALS-g2	Abrupt
LASG/IAP, China	FGOALS	FGOALS-s2	Abrupt
Geophysical Fluid Dynamics Laboratory, United States	GFDL	GFDL CM3	Abrupt and transient
Geophysical Fluid Dynamics Laboratory, United States	GFDL	GFDL-ESM2G	Abrupt
Geophysical Fluid Dynamics Laboratory, United States	GFDL	GFDL-ESM2M	Abrupt
Goddard Institute for Space Studies, United States	GISS	GISS-E2-H	Abrupt
Goddard Institute for Space Studies, United States	GISS	GISS-E2-R	Abrupt and transient
Institute of Numerical Mathematics, Russia	INM	INM-CM4.0	Abrupt and transient
L'Institut Pierre-Simon Laplace, France	IPSL	IPSL-CM5A	Transient
L'Institut Pierre-Simon Laplace, France	IPSL	IPSL-CM5A-LR	Abrupt
L'Institut Pierre-Simon Laplace, France	IPSL	IPSL-CM5B-LR	Abrupt
L'Institut Pierre-Simon Laplace, France	IPSL	IPSL-CM5A-MR	Abrupt
Model for Interdisciplinary Research on Climate/Atmosphere and Ocean Research Institute (AORI), The University of Tokyo/National Institute for Environmental Studies (NIES)/JAMSTEC, Japan	MIROC	MIROC5	Abrupt and transient
Model for Interdisciplinary Research On Climate/AORI, The University of Tokyo/NIES/JAMSTEC, Japan	MIROC	MIROC-ESM	Transient
Max Planck Institute, Germany	MPI	MPI-ESM-LR	Abrupt and transient
Max Planck Institute, Germany	MPI	MPI-ESM-MR	Abrupt
Max Planck Institute, Germany	MPI	MPI-ESM-P	Abrupt
Meteorological Research Institute, Japan	MRI	MRI-CGCM3	Abrupt and transient
National Center for Atmospheric Research, United States	NCAR	CCSM4	Abrupt and transient
Norwegian Climate Centre (NCC), Norway	NCC	NorESM1	Transient
Met Office Hadley Centre, United Kingdom	MOHC	HadGEM2-ES	Abrupt and transient

The CMIP5 data used in this study are summarized in Table 1. Data from three sets of experiments are analyzed: the abrupt $4 \times CO_2$ experiments as mentioned, the preindustrial control experiments that are subtracted from the abrupt experiment to remove drift following the approach of DeAngelis et al. (2015), and the transient climate change experiment with the model forced by a 1% yr^{-1} increase in CO_2. The transient experiment is used to examine the more realistic changes that might be expected to occur in an evolving climate system. Results of the transient experiment for one model (HadGEM2-ES) are shown in Fig. 1 mostly for the purpose of illustration and framing the later discussion. For this one example, differences between the averages over the final 5 years of the experiment (years 136–140, or 1999) and the first 5 years (years 0–4, or 1860) are shown. Over the period of time that elapses between these two 5-yr averages, the CO_2 of the model approximately quadrupled and the modeled earth warmed everywhere as indicated by the change in near-surface air temperature (SAT; Fig. 1, top left). Changes in OLR (Fig. 1, top right) and clear-sky OLR (Fig. 1, bottom left) reveal that,

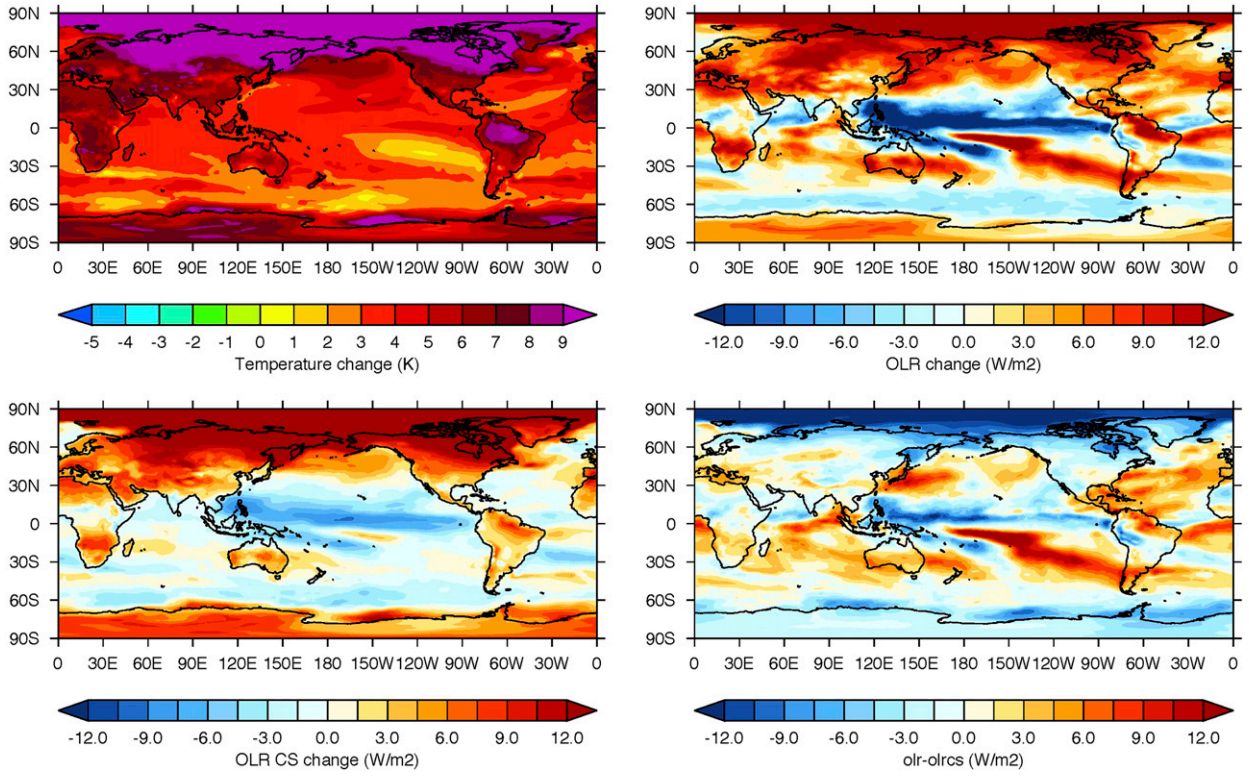

FIG. 1. Differences of quantities averaged over the years 136–140 (1999) and 0–4 (1860) of the CMIP5 1% yr^{-1} increased CO_2 transient experiment. Quantities shown are the (top left) SAT, (top right) OLR, (bottom left) clear-sky OLR, and (bottom right) the change in the longwave cloud radiative effects (the difference between and the clear- and all-sky OLRs). The results shown are for the HadGEM2-ES.

unlike SAT, neither the all-sky nor the clear-sky OLR increases systematically everywhere with warming. These regions of reduced emission tend to be offset by enhanced emission to space in the middle-to-higher latitudes, most notably over the warmed landmasses of the NH. This pattern of negative changes in OLR at low latitudes and positive changes at higher latitudes is largely a manifestation of the feedbacks involving an enhanced greenhouse associated with upper-tropospheric water vapor at low latitudes and the so-called Planck feedback associated with a warmed atmosphere at higher latitudes. The general effect of clouds on the OLR, indicated by the clear-sky minus all-sky OLR differences in the bottom-right panel of Fig. 1, at least for HadGEM2-ES, amplifies the clear-sky pattern of change. This amplification of the pattern is also apparent in the multimodel results of Andrews et al. (2015) and is discussed in the following section.

3. The SGE

An assumption inherent to (5) is that feedbacks are constant over the time period analyzed. Andrews et al. (2015) showed how the feedbacks, although largely linear, vary in time and appear to separate into a relatively fast response epoch (up to the first 20 years) and a slower response epoch from years 21 to 150. Feedback analyses are applied to data from each of these two epochs as well as to the total time period and are summarized in Fig. 2 for the HadGEM2-ES model and Fig. 3 for the multimodel mean. Figures 2 and 3 are constructed as six panels showing the all-sky LW feedbacks (top panels) and clear-sky LW regional feedbacks (bottom panels). In all cases, the pattern of feedback is similar, although the magnitude and areal extent of the SGE region varies. The pattern of positive feedback in Fig. 3 closely resembles the regions of negative OLR change noted in Fig. 1, which is expected because these regions of negative OLR change in the transient experiment are primarily set by feedbacks.

Figures 4a–c summarize the LW feedbacks in zonally averaged form for both epochs and for all sky, clear sky, and the difference between them. In the bulk sense and at most latitudes, the LW cloud feedbacks are all positive acting to reduce the clear-sky feedbacks at all latitudes except those that straddle the tropical heating region of the SGE. The maps of Figs. 2 and 3 clearly show an enhanced all-sky negative feedback response both poleward and to the west of the enhanced positive

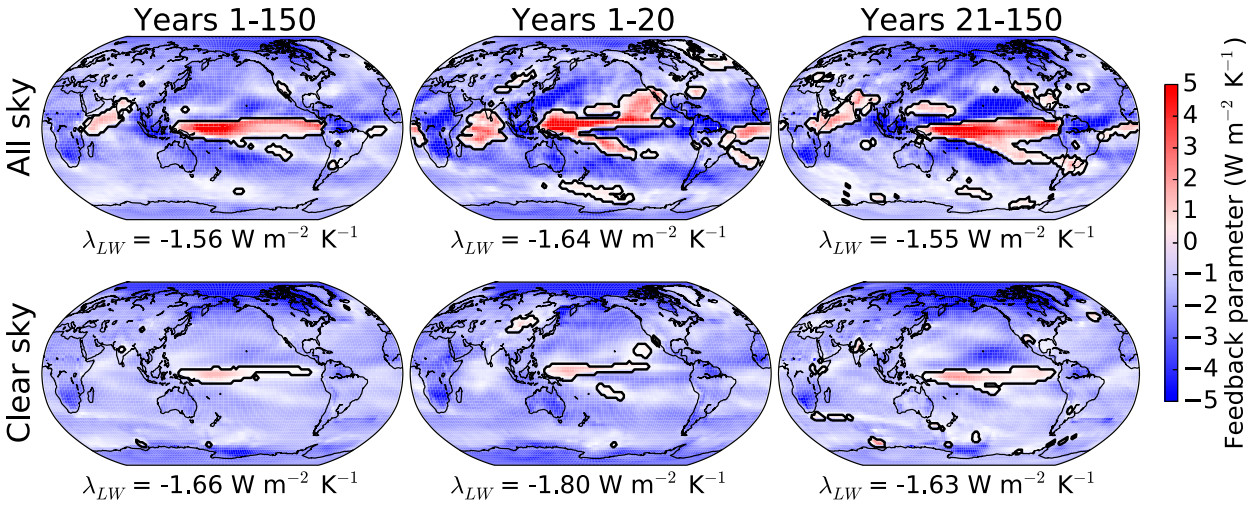

FIG. 2. The (top) all-sky and (bottom) clear-sky longwave feedbacks for (left)–(right) three different periods of time for HadGEM2-ES. The zero feedback contour is highlighted in black to delineate the positive (red) and negative (blue) feedbacks.

SGE feedback, which is very analogous to the dynamical response to an equatorial heating described by Gill (1980). Figure 4d also provides the ratio of all sky to clear sky of the accumulated heat calculated by integrating over regions of positive α for latitudes between 20°N and 20°S. The ratio is presented for the two epochs (years 0–20 in red and 21–150 in blue). Clouds substantially enhance the SGE effect by a factor of 10.7 in years 1–20 and 7.4 in years 21–150. The model-to-model range of this amplification is large, suggesting that the magnitude of the cloud feedback is also highly uncertain.

4. Forcing and feedback influences on the OLR under the 1% yr^{-1} CO_2 scenario

The quadrupling of CO_2 through the course of the model integrations imposes an influence on the OLR that is implicit in the OLR differences shown in Fig. 1. To determine this contribution, calculations were performed with an offline radiation model (Stephens et al. 2001) that has been verified against observations (e.g., L'Ecuyer et al. 2008) and has served as the basis of the *CloudSat* fluxes product (Henderson et al. 2013). The radiation model is a derivative of the widely used Fu and Liou scheme (Fu and Liou 1992). Monthly mean temperature, moisture, and profile data from both the initial and end periods of the 1% yr^{-1} experiment for HadGEM2-ES served as input to this offline model.

Several sets of calculations of clear-sky OLR were performed. First the clear-sky OLR was calculated using atmospheric profiles from the 1860 period assuming two different concentrations of CO_2, one corresponding to the initial 280 ppm and the second corresponding to its

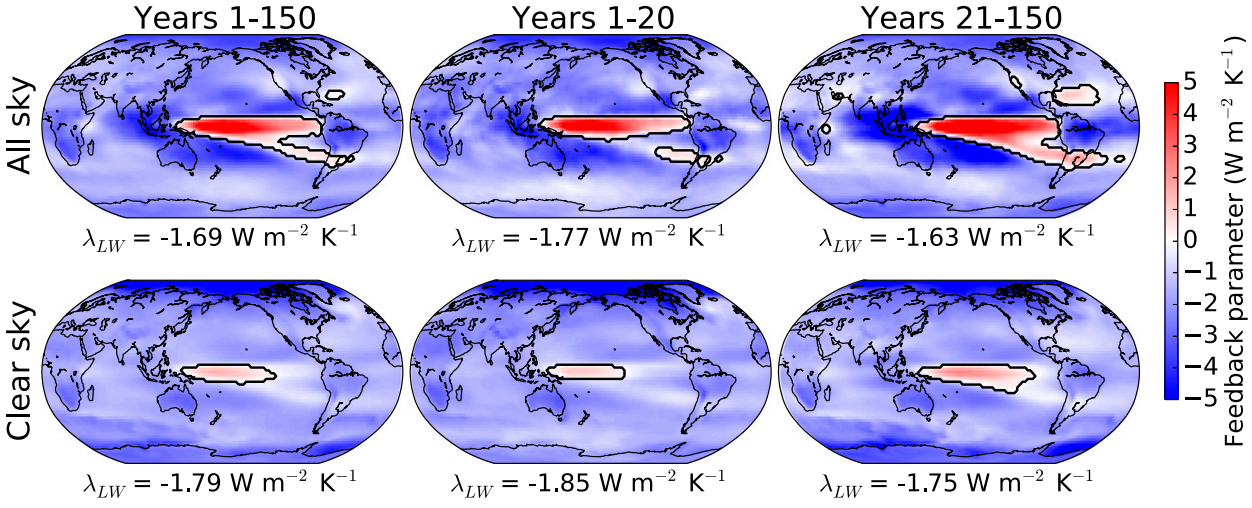

FIG. 3. As in Fig. 2, but for the 26-model mean.

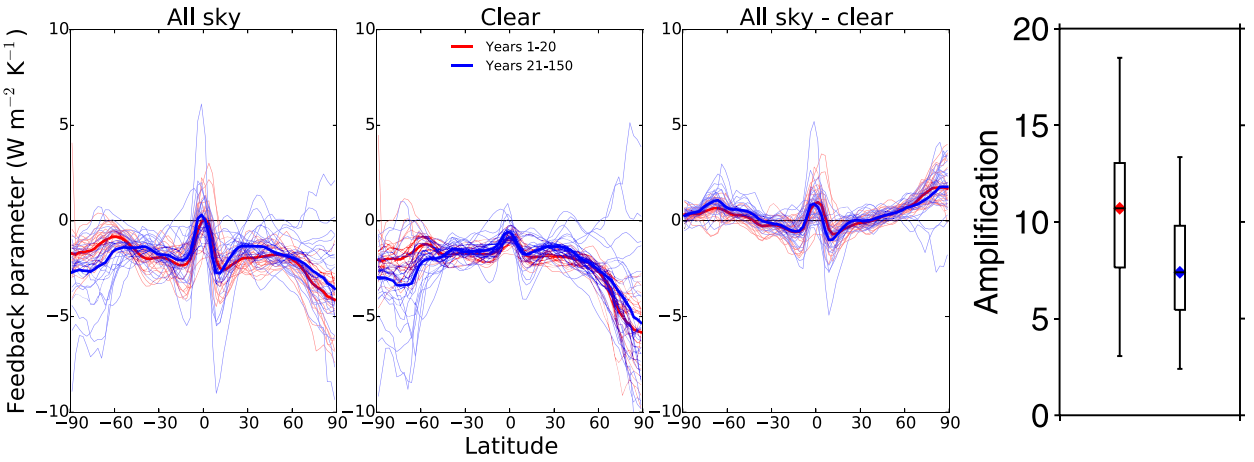

FIG. 4. Zonal averaged feedback for (a) all sky, (b) clear sky, and (c) their differences. Bold lines are the 26-model ensemble average with years 1–20 (red) and 21–150 (blue); individual model results are presented as thin lines. Clouds are largely a source of positive feedback on OLR. (d) Box-and-whisker plot of area-weighted all-sky feedback (W m^{-2} K^{-1}) divided by clear-sky feedback within SGE regions, showing that clouds amplify the clear-sky SGE.

quadrupled value (Fig. 5a). The 4 × CO_2 minus 1 × CO_2 OLR calculated difference is the instantaneous radiative forcing and closely matches the forcing calculated from the abrupt 4 × CO_2 experiments reported in Andrews et al. (2015). The distribution of this flux difference in Fig. 5a essentially reproduces the multimodel instantaneous forcing summarized in Zhang and Huang (2014). The distribution of the OLR difference from CO_2 exhibits distinct structure that, among other factors, reflects the pattern of upper-tropospheric humidity, with the largest values aligning with the drier regions of the subtropics and smaller values in the moist tropics. This is to be expected because the changes in emission associated with a CO_2 increase overlap with water vapor emission from the strongly absorbing water rotation band. Thus, changes in emission by CO_2 are more highly masked by the emission from water vapor in the moister regions of the tropics.

Figure 5b presents the OLR calculated for 1 × CO_2 and the atmospheric state of 1860 but with the temperatures replaced by the 1999 distribution minus the 1860 OLR. This difference thus represents the effects of the 4 × CO_2 temperature increase alone on OLR. The changes in OLR are positive everywhere, especially over NH landmasses, and are significantly larger than the OLR decrease associated with the CO_2 forcing as was shown in Andrews and Ringer (2014). Figure 5c shows the sum of the temperature and 4 × CO_2 impacts on the OLR. The patterns are generally similar to temperature alone (Fig. 5b) but are reduced in magnitude. Figure 5c confirms the dominance of temperature change over the CO_2 forcing except in the region of the Southern Ocean where the CO_2 forcing remains a significant contributor to the derived OLR change.

Figure 5d is analogous to Fig. 5b except the water vapor difference from 1999 to 1860 is shown with temperatures held at 1860. The clear-sky OLR is reduced everywhere with the largest reductions in the most convectively active areas of the tropics. Figure 5e shows the sum of Figs. 5b and 5d, and negative regions represent the SGE with respect to the temperature and water vapor feedbacks only. Figure 5f is similar to Fig. 5e but includes the contributions of 4 × CO_2 forcing added to the feedbacks. Negative regions show the SGE regions with respect to the sum of forcing and feedbacks together. Comparison of Figs. 5e and 5f reveals the dominance of the water vapor feedbacks on shaping the spatial patterns of the OLR differences everywhere and especially in the moist tropical regions. Even over the Southern Ocean regions where the CO_2 forcing is important to the OLR response, the water vapor feedback is also an important contributor. The CO_2 forcing increases the spatial coverage of the SGE regions where the temperature and water vapor feedback contributions to clear-sky OLR changes are similar in magnitude.

5. The structural character of the clear-sky SGE

We show below how the clear-sky SGE is a fundamental source of heating of the climate system. Here we examine the factors that are largely responsible for the changes to the clear-sky OLR depicted in Fig. 1. For this purpose, we adopt a simple sensitivity analysis similar to that described in Dessler et al. (2008). The sensitivity of

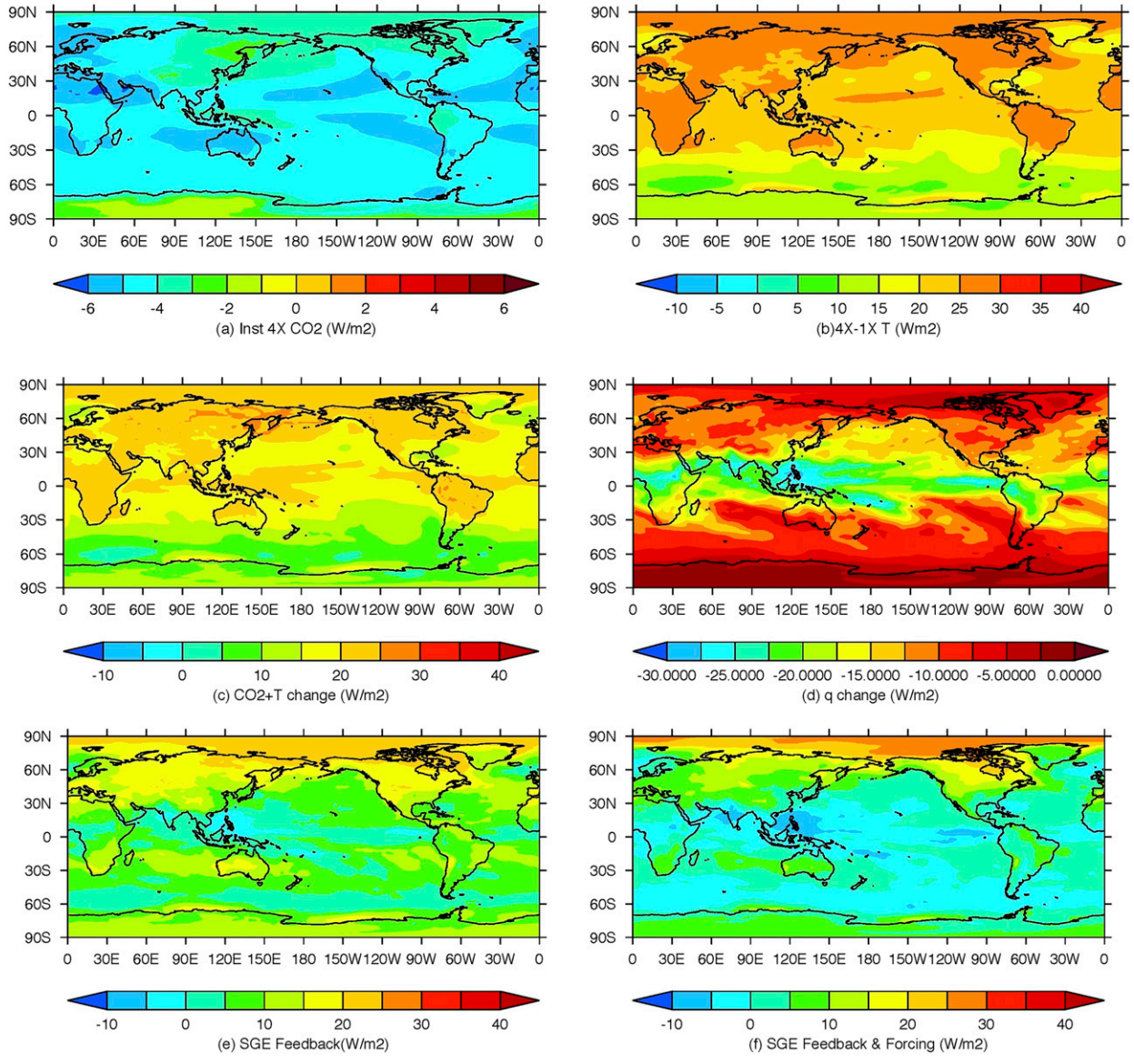

FIG. 5. Clear-sky OLR differences: (a) the $4 \times CO_2$ minus $1 \times CO_2$ OLR difference calculated for the 1860 model climate state; (b) as in (a), but with the temperature replaced with 1999 values; (c) the sum of (a) and (b); (d) as in (b), but for water vapor; (e) OLR change from feedbacks only; (f) OLR change from feedbacks and forcing. All results apply to HadGEM2-ES and were calculated with an offline radiative transfer model.

the clear-sky OLR to changes in altitude-resolved atmospheric temperature T_a and water vapor q, expressed as $\partial \mathrm{OLR}/\partial T_a$ and $\partial \mathrm{OLR}/\partial q$, are given in Fig. 6. In constructing this plot, T_a and q profiles from the Atmospheric Infrared Sounder (AIRS; Chahine et al. 2006) collected in 2012 were averaged into 1-K sea surface temperature T_s bins. These profiles were then used as input into the same radiation model used to produce the CO_2 flux difference plots described above. Of the 12 longwave infrared bands of the model, 8 are located in the mid IR ($\lambda < 15\,\mu$m) with the remaining four bands located in the far IR ($\lambda > 15\,\mu$m). The bin-averaged T_a and q profiles were then respectively perturbed by +1 K and +10% in each 100-hPa-thick layer, and a new OLR was then calculated for perturbations to each 100-hPa layer of mean pressure p and for each surface temperature bin T_s. In this way, the OLR sensitivities are created as functions of p and T_s and are also calculated separately for broadband OLR ($\mathrm{OLR_{bb}}$; $\lambda > 4\,\mu$m), the sum of the four far-IR OLR bands $\mathrm{OLR_{far}}$ ($\lambda > 15\,\mu$m), and the sum of the eight mid-IR OLR bands $\mathrm{OLR_{mid}}$ ($\lambda < 15\,\mu$m).

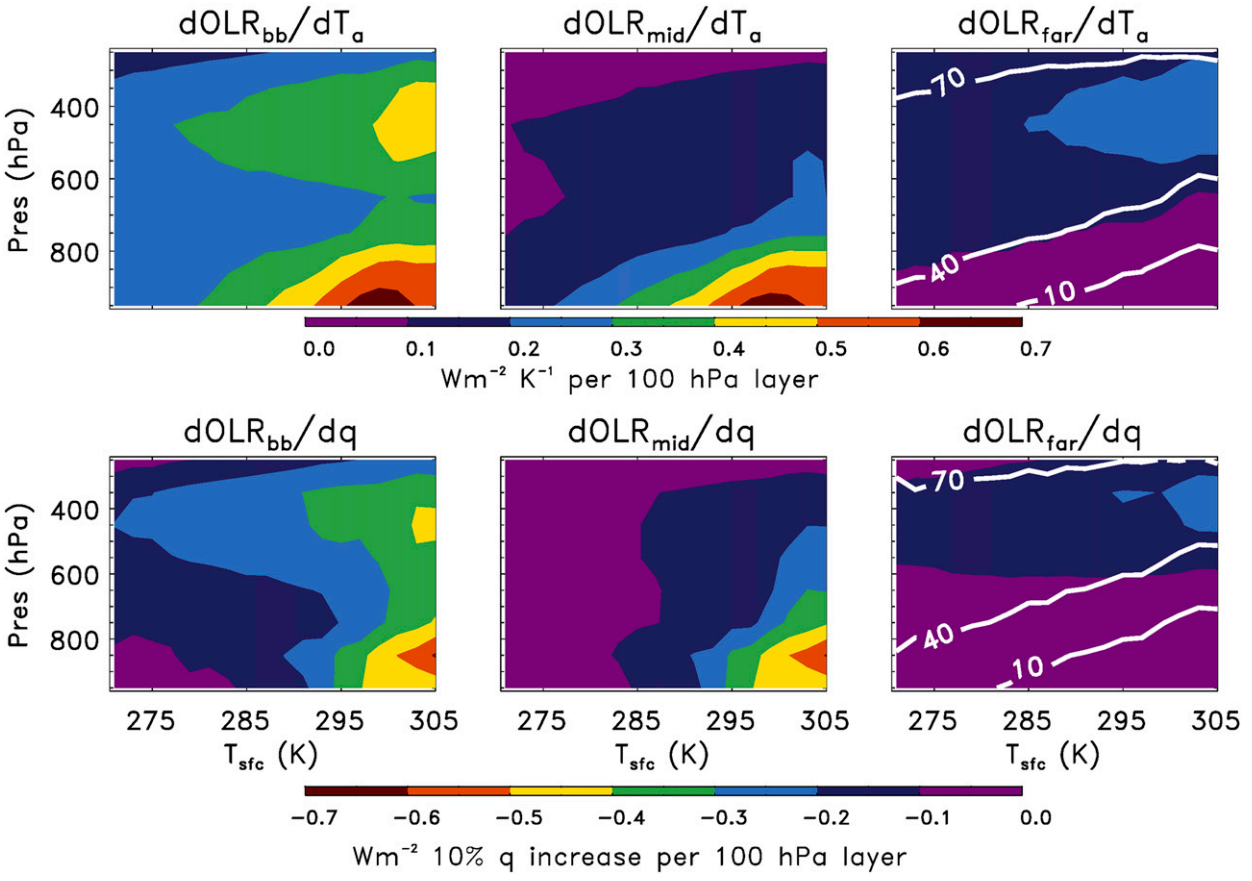

FIG. 6. (left)–(right) The broadband-, mid-, and far-IR sensitivity of the OLR as a function of sea surface temperature T_{sfc}. These sensitivities are derived from calculations for (top) 1-K atmospheric temperature T_a and (bottom) 10% water vapor mixing ratio q perturbations applied to 100-hPa layers. The perturbations are from a mean climatological state taken from the AIRS clear-sky retrievals during 2012. Superimposed on the far-IR sensitivities are contours of the fractional contributions of the far IR to the total OLR sensitivity.

The top panels of Fig. 6 are the OLR sensitivities to T_a, and the bottom panels show sensitivities to q. The sensitivities of spectral and broadband OLR to increased T_a are positive everywhere. The maximum T_a sensitivity of the mid IR occurs in the lower atmosphere over regions of highest T_s. By contrast, the maximum temperature sensitivity of the far IR is located in the upper troposphere and also in regions of higher T_s. These two factors combine to produce a broadband sensitivity (viz., $\partial \mathrm{OLR}_{\mathrm{bb}}/\partial T_a$) that is bimodal in altitude at these higher surface temperatures.

In contrast to the T_a sensitivities, the sensitivities of broadband, mid, and far IR to changes in q are negative everywhere with a structure that is similar to the temperature sensitivities. For example, the maximum q sensitivity in the mid IR occurs in the lower atmosphere and over warmer surfaces, whereas the maximum in far-IR sensitivity, like temperature, occurs in the upper troposphere, although the peak sensitivity of q is located at slightly higher altitudes than are the T_a sensitivities. The assumed moistening (+10%) and warming (+1 K) applied in Fig. 6 demonstrate the relative response across a range of T_s and altitude. With a much larger relative increase in q compared to T_a, which is a more realistic representation in the heart of the tropical SGE regions, the reduction in OLR will be much larger and well explains the patterns observed in Figs. 1, 2, 3, 5e, and 5f.

In a warming planet, increased temperatures occur synchronously with increased water vapor, so the net OLR response is some weighted combination of the sensitivities shown in Fig. 6. Consequently, the spatial distribution of change is more complex than that given by simple and separate perturbations of +1 K in T_a and +10% in q as used for Fig. 6. This complexity is seen in both satellite observations of multiyear variability and climate model simulations of multidecadal trends. Gambacorta et al. (2008) used ENSO variations of AIRS T_a and q soundings as a proxy for present-day climate variability and showed regions of drying, as well

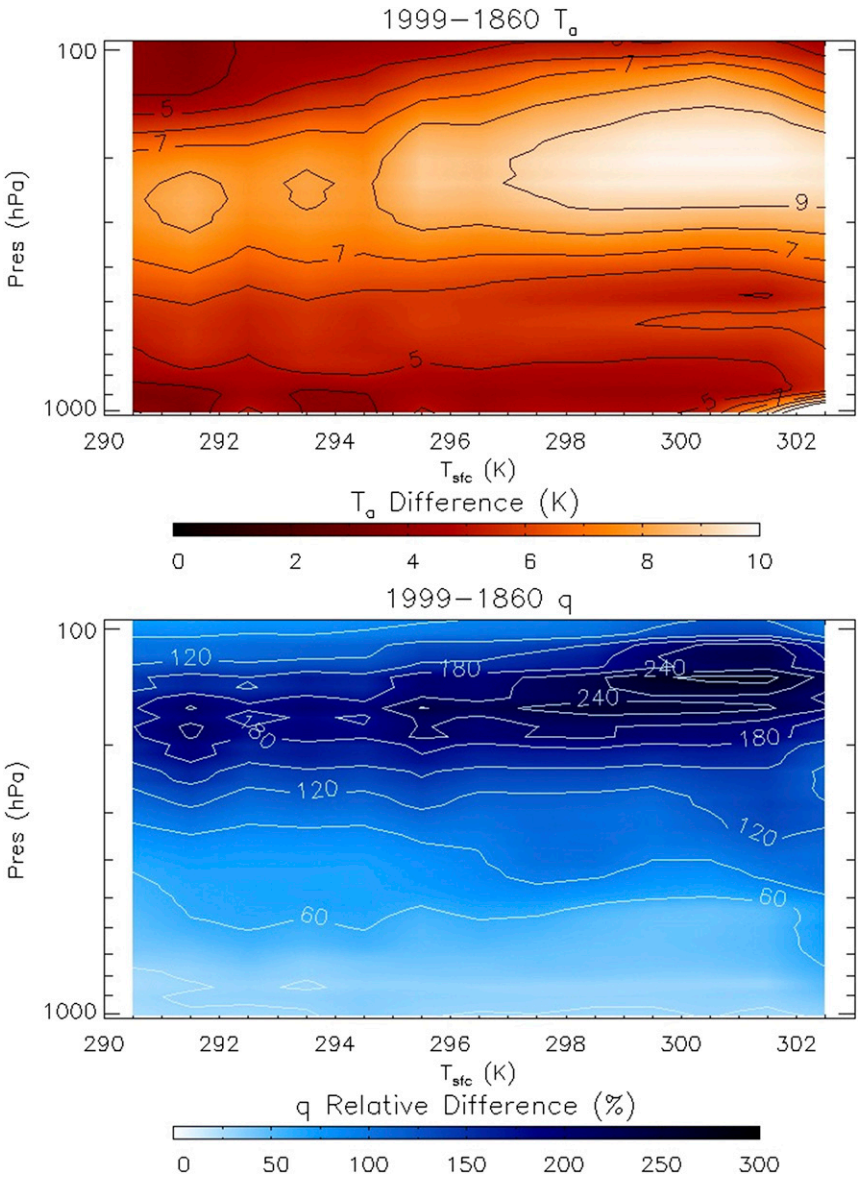

FIG. 7. (top) The difference profiles of T_a and (bottom) the relative difference of q for 1999–1860 of the 1% yr^{-1} HadGEM2-ES experiments.

as moistening, within many tropical and subtropical upper-tropospheric regions that are several times higher than predicted by the Clausius–Clapeyron relation (7% K^{-1}). Similar regional variations that deviate strongly from the global mean in the long-term rate of upper-tropospheric moistening are also observed in climate model simulations (Sherwood et al. 2010). The nature of this complication is revealed in Fig. 7 showing the difference profiles of 1999–1860 for the 1% yr^{-1} HadGEM2-ES experiments. The difference in the mean T_a and q fields indicates that some regions of the lower and middle subtropical and tropical troposphere dry and warm in contrast to the more dramatic moistening and warming found in the upper troposphere. The combination of T_a and q perturbations and their effect on OLR is presented in Fig. 8, symbolically $\partial \mathrm{OLR}/\partial T_a + \partial \mathrm{OLR}/\partial q$, calculated from the respective joint T_a and q perturbations of individual layers obtained. The combined sensitivities for the broadband, mid, and far IR are presented and emphasize how synchronous changes in T_a and q combine to affect the clear-sky OLR. The results of Figs. 6 and 8 suggests that the SGE that can be readily identified in Figs. 1, 2, and 3 is a consequence of the moistening of the upper troposphere (e.g., Fig. 6, bottom) over the warmest regions of the planet that is shaped by

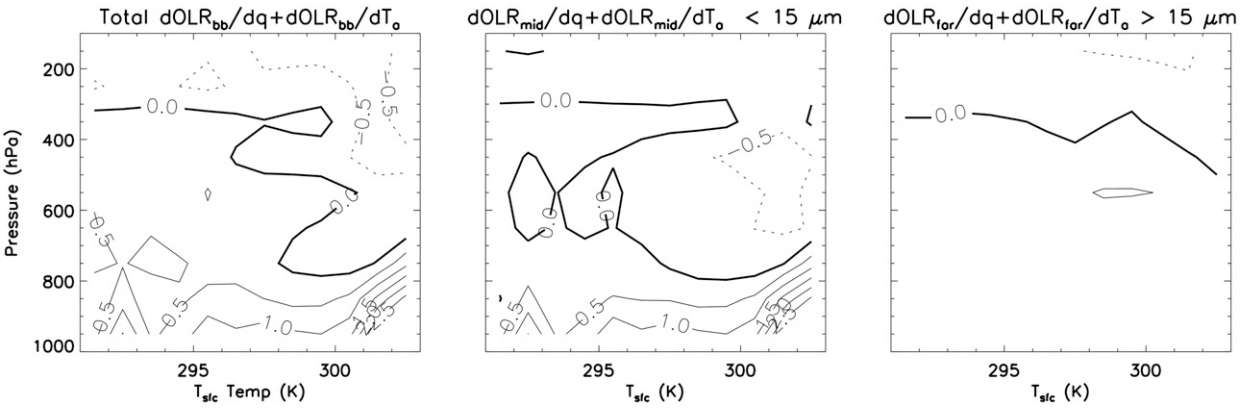

FIG. 8. As in Fig. 6, but for the combined changes of T_a and q. The changes in these properties are those taken from Fig. 6 and input into a radiation model to calculate the sensitivities. The units are in W m^{-2} per 100-hPa layer for a sum of a 10% increase in q and +1-K increase in T_a.

emission changes in the far IR (Fig. 8, right) but with nonnegligible contributions in mid-IR emission from the midtroposphere over the warmest regions of the planet where SAT > 300 K. Furthermore, Figs. 6 and 8, in addition to Fig. 5, illustrate that the increased OLR at higher latitudes is largely a consequence of temperature changes in these regions.

6. Global implications

The pattern of OLR change presented in Fig. 1, with the SGE in low latitudes and the increased emission at higher latitudes that is caused by a combination of feedback and forcing, suggests that these infrared radiation processes act together to enhance transport of heat poleward with the increased heating at low latitudes transported to balance the enhanced energy loss at high latitudes. However, it is the latitudinal distribution of the TOA net radiative flux and not any individual flux contribution that determines the overall amount of heat transported. Here we examine how the meridional transport changes in the 1% yr^{-1} experiments and provide an assessment of the specific influences of the changes in OLR on this transport.

We first examine the global and hemispheric energy imbalances derived from the annual-mean TOA radiation balances of the models. This imbalance is calculated as the differences in TOA balance between 1860 and 1999 and is shown in Fig. 9 as a multimodel average with a standard deviation to indicate the spread within the model ensemble. Between 1860 and 1999, the average global heat storage of the 14 models analyzed is 1.03 ± 0.2 PW.

The usual practice of using the annual-mean TOA radiation balance to calculate the meridional transport of heat requires the assumption that the heat stored within the system on the annual mean is negligible. This

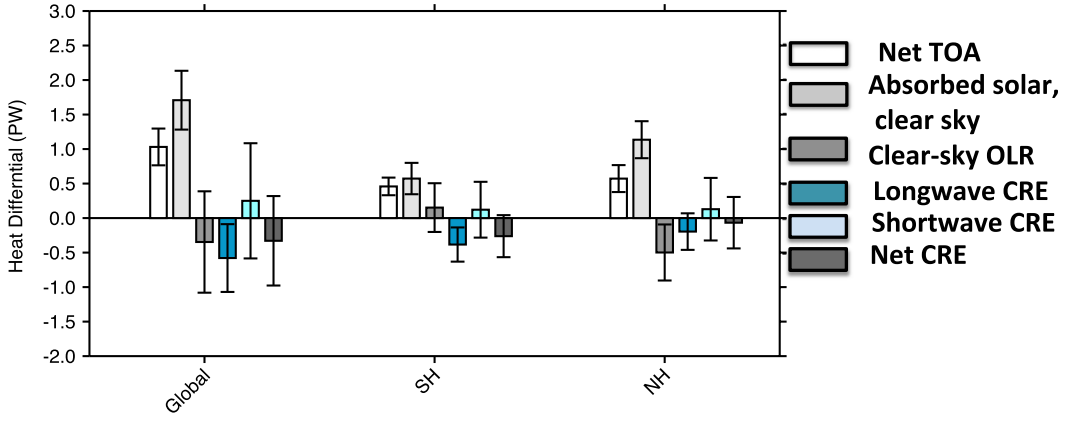

FIG. 9. Differences of multimodel mean net TOA fluxes and the component fluxes averaged over 1999 and 1860 of the CMIP5 1% yr^{-1} increased CO_2 transient experiment. The flux differences are integrated globally and over each hemisphere. The error bars indicate variability of the multimodel ensemble.

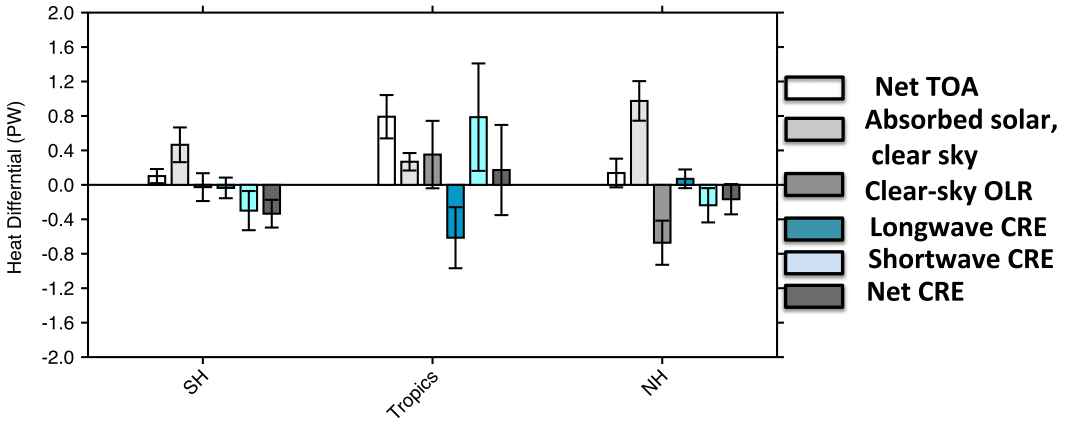

FIG. 10. As in Fig. 9, but for the multimodel mean TOA flux differences integrated over the three regions of the globe delineated by the latitudes of the zero annual-mean net flux.

assumption no longer holds for these forced climate experiments analyzed, and rather than employ ambiguous regional adjustments for the small amount of heat stored, we choose to avoid this ambiguity and use specific properties of the TOA net flux that relate specifically to the meridional heat transport. This approach for diagnosing the main properties of the heat transport is discussed in Stephens et al. (2015). The latitudes of zero zonally averaged net TOA flux are the latitudes where maximum transport of heat occurs in each hemisphere. The integrated losses of energy poleward of these latitudes define the magnitudes of the maximum transports. Thus, the three main regions of the planet delineated by these two zero net TOA flux latitudes define the three main regions that are most directly related to the transport of heat poleward. The regions equatorward of the zero net flux latitudes (hereafter the tropics) is the region where the absorbed solar radiation accumulates heat at a rate that exceeds the ability of the system to radiate this energy back to space by longwave radiation. This equatorial region is fundamentally unstable and implies a runaway earth in the absence of horizontal transport of heat out of these unstable zones. This transport is required to maintain a stable equilibrium (Bates 1999; Pierrehumbert 1995).

Since the net TOA fluxes of these three regions directly relate to the properties of the meridional heat transport, it is then possible to determine how the different TOA flux components, or changes to them, influence this transport and subsequent changes to the transport. These flux contributions in turn point to the processes that are important in shaping the heat transport. This is investigated in Fig. 10 showing the individual flux component contributions to the changes in heat uptake in lower latitudes (the tropics) and loss of heat at higher latitudes (the extratropics), each region being separately calculated from each model. Contributions to changes in heat contents by changes in clear-sky long- and shortwave fluxes and by cloudy-sky fluxes are determined for each region. In this way the specific contributions of the SGE and other radiative processes on heat transport are explicitly revealed. As in Fig. 9, the results presented in Fig. 10 are in the form of a histogram and show the multimodel mean and the spread of the differences between 1999 and 1860. The main findings of this analysis are the following:

(i) Most of the 1.03 PW of heat accumulated in the modeled earth (Fig. 9) occurs in the tropical region where 0.8 PW of heat is absorbed (Fig. 10). This buildup of heat in the tropics is contributed almost equally by reductions in clear-sky longwave emission (i.e., the clear-sky SGE) and increased absorbed clear-sky solar radiation associated with greater amounts of water vapor (Stephens and Hu 2010; Donohoe et al. 2014). Thus, the processes that define the clear-sky SGE are fundamental to the way models accumulate heat and also to how much heat is then transported poleward. The increased heat uptake at low latitudes and the resulting increased transport of heat to higher latitudes was also noted in Zelinka and Hartmann (2012).

(ii) The cloud influences on the heat accumulated at low latitudes, as is common to most cloud radiative effects in the tropics, is a result of largely canceling long- and shortwave effects leaving a relatively small gain in solar heating that is consistent with a predominantly positive cloud feedback operating in models (IPCC 2013) associated with subtropical low cloud changes. The largest differences between the models are the cloud radiative effects in these tropical latitudes.

(iii) The higher-latitude extratropics are also slightly heated resulting in small reductions to the higher-latitude net heat losses (0.10 PW in the SH and

0.13 PW in the NH). Since the maximum heat transported poleward in each hemisphere is set by the energy loss in the extratropics, this implies an overall slight reduction of the maximum meridional heat transport in the warmed earth by these respective amounts. This reduced heat loss of the extratropics, and the reduction in maximum heat transported poleward, occurs in each hemisphere through very different mechanisms. While considerable increased heating of the NH extratropics occurs almost equally from increased clear-sky solar absorption from the positive feedback associated with reductions in snow and ice cover (e.g., Andrews et al. 2015), the enhanced emission to space from the warmed higher latitudes largely offsets this increased clear-sky solar absorption. This increased loss is further added to by reduced solar absorption associated with increased cloud cover. In the SH, the increased clear-sky absorption associated with sea ice reductions is mostly offset by increased solar reflection by clouds also presumably associated with increases of SH cloudiness.

7. Summary and conclusions

This paper extends the concept of the super greenhouse effect (SGE) within the context of climate change. The SGE is not simply defined by an SST threshold as in previous studies but is derived from feedback analysis of the World Climate Research Programme's (WCRP) phase 5 of the Coupled Model Intercomparison Project (CMIP5) abrupt $4 \times CO_2$ experiments. The properties of the SGE and its influence on the broader climate system with anthropogenic forcing are also explored using model data available from the $1\%\ yr^{-1}$ increasing CO_2 transient experiments.

The main findings in relation to the SGE are the following:

(i) In all models, there are regions in the low latitudes, typically between 20°N and 20°S, where the clear-sky and all-sky OLR decrease with surface warming. These are identified as regions of positive longwave feedback and regions of a SGE dominated by the water vapor feedbacks and upper-tropospheric clouds. Conversely, the OLR in higher latitudes increases along with increasing temperatures except over the southern oceans (Figs. 1 and 5).

(ii) The general effects of clouds on the SGE are to amplify the clear-sky SGE, but there is little agreement on the magnitude of this amplification. In the 20°N and 20°S region, the SGE amplification of clouds varies by almost an order of magnitude among the models considered (Fig. 4d), which may be symptomatic of large model differences in how convective parameterizations contribute to upper-tropospheric moistening.

(iii) Sensitivity analysis of the clear-sky OLR indicates that the spatial extent of the SGE regions are a consequence of the moistening of the upper troposphere (e.g., Fig. 5e) over the warmest regions of the planet that is shaped by emission changes in the far IR (Fig. 8, right) but with nonnegligible contributions from mid-IR emission from the midtroposphere over the warmest regions of the planet where SAT > 300 K.

(iv) The change in OLR over the Southern Ocean is particularly interesting and warrants more research. As most models predict, the smallest warming is found over the Southern Oceans, and as described earlier, its change to OLR has important residual contributions from the CO_2 forcing.

These results were placed into the broader context of meridional heat transport from low to high latitudes. A simple analysis of heat transport was introduced based on specific properties of the TOA net flux that relate specifically to the meridional heat transport. This avoided introducing assumptions about how to partition the imbalance in the TOA energy budget while also providing the means for examining how different radiative processes, such as those associated with the SGE, affect heat transport. The main findings of this part of the analysis were the following:

(i) Most of the 1.03 PW of heat accumulated in the modeled earth (Fig. 9) occurs in the tropical region where 0.8 PW of heat is absorbed. This buildup of heat in the tropics is contributed almost equally by reductions in clear-sky longwave emission (i.e., the clear-sky SGE) and increased absorbed clear-sky solar radiation associated with greater amounts of water vapor. This increase in heat absorbed in low latitudes requires an enhanced meridional transport of heat from these regions to maintain climate stability.

(ii) The higher-latitude extratropics are also slightly heated resulting in small reductions to the higher-latitude net heat losses (0.10 PW in the SH and 0.13 PW in the NH). Since the maximum heat transported poleward in each hemisphere is set by the energy loss in the extratropics, this implies a slight reduction in the maximum of the meridional heat transport in the warmed earth by these respective amounts. This reduced heat loss of the extratropics occurs in each hemisphere through very different mechanisms.

Acknowledgments. The HadGEM2-ES data used for the offline calculations was furnished by Alejandro Bodas-Salcedo of the UKMO. The authors and content of the paper also benefited from discussions with Tim Andrews of the UKMO and in particular Kyle Armour of the University of Washington. The research described in this paper was carried out at the Jet Propulsion Laboratory (JPL), California Institute of Technology, under a contract with the National Aeronautics and Space Administration. The AIRS version 6 datasets were processed by and obtained from the Goddard Earth Services Data and Information Services Center (http://daac.gsfc.nasa.gov/; Teixeira et al. 2013). The JPL author's copyright for this publication is held by the California Institute of Technology. Government sponsorship acknowledged.

REFERENCES

Andrews, T., and M. Ringer, 2014: Cloud feedbacks, rapid adjustments, and the forcing–response relationship in a transient CO_2 reversibility scenario. *J. Climate*, **27**, 1799–1818, doi:10.1175/JCLI-D-13-00421.1.

——, J. M. Gregory, and M. J. Webb, 2015: The dependence of radiative forcing and feedback on evolving patterns of surface temperature change in climate models. *J. Climate*, **28**, 1630–1648, doi:10.1175/JCLI-D-14-00545.1.

Arrhenius, S., 1896: On the influence of carbonic acid in the air upon the temperature of the ground. *Philos. Mag.*, **41**, 237–276, doi:10.1080/14786449608620846.

Bates, R., 1999: A dynamical stabilizer in the climate system: A mechanism suggested by a simple model. *Tellus*, **51A**, 349–372, doi:10.1034/j.1600-0870.1999.t01-3-00002.x.

Bornemann, A., and Coauthors, 2008: Isotopic evidence for glaciation during the Cretaceous supergreenhouse. *Science*, **319**, 189–192, doi:10.1126/science.1148777.

Chahine, M. T., and Coauthors, 2006: The Atmospheric Infrared Sounder (AIRS): Improving weather forecasting and providing new insights into climate. *Bull. Amer. Meteor. Soc.*, **87**, 911–926, doi:10.1175/BAMS-87-7-911.

Chung, E.-S., B. Soden, B. J. Sohn, and L. Shi, 2014: Upper-tropospheric moistening in response to anthropogenic warming. *Proc. Natl. Acad. Sci. USA*, **111**, 11 636–11 641, doi:10.1073/pnas.1409659111.

DeAngelis, A. M., X. Qu, M. D. Zelinka, and A. Hall, 2015: An observational radiative constraint on hydrologic cycle intensification. *Nature*, **528**, 249–253, doi:10.1038/nature15770.

Dessler, A. E., and S. M. Davis, 2010: Trends in tropospheric humidity from reanalysis systems. *J. Geophys. Res.*, **115**, D19127, doi:10.1029/2010JD014192.

——, P. Yang, J. Lee, J. Solbrig, and K. Minschwaner, 2008: An analysis of the dependence of clear-sky top-of-atmosphere outgoing longwave radiation on atmospheric temperature and water vapor. *J. Geophys. Res.*, **113**, D17102, doi:10.1029/2008JD010137.

——, M. R. Schoeberl, T. Wang, S. M. Davis, and K. H. Rosenlof, 2013: Stratospheric water vapor feedback. *Proc. Natl. Acad. Sci. USA*, **110**, 18 087–18 091, doi:10.1073/pnas.1310344110.

Donohoe, A., K. C. Armour, A. G. Pendergrass, and D. S. Battisti, 2014: Shortwave and longwave radiative contributions to global warming under increasing CO_2. *Proc. Natl. Acad. Sci. USA*, **111**, 16 700–16 705, doi:10.1073/pnas.1412190111.

Fourier, J., 1824: Remarques générales sur les températures du globe terrestre et des espaces planétaires (General remarks on the temperature of the Earth and outer space). *Ann. Chem. Phys.*, **27**, 136–167.

Fu, Q., and K. N. Liou, 1992: On the correlated *k*-distribution for radiative transfer in nonhomogeneous atmospheres. *J. Atmos. Sci.*, **49**, 2139–2156, doi:10.1175/1520-0469(1992)049<2139:OTCDMF>2.0.CO;2.

Gambacorta, A., C. Barnet, B. Soden, and L. Strow, 2008: An assessment of the tropical humidity-temperature covariance using AIRS. *Geophys. Res. Lett.*, **35**, L10814, doi:10.1029/2008GL033805.

Gill, A. E., 1980: Some simple solutions for heat-induced tropical circulation. *Quart. J. Roy. Meteor. Soc.*, **106**, 447–462, doi:10.1002/qj.49710644905.

Gregory, J. M., and Coauthors, 2004: A new method for diagnosing radiative forcing and climate sensitivity. *Geophys. Res. Lett.*, **31**, L03205, doi:10.1029/2003GL018747.

Hallberg, R., and A. K. Inamdar, 1993: Observations of seasonal variations in atmospheric greenhouse trapping and its enhancement at high sea surface temperature. *J. Climate*, **6**, 920–931, doi:10.1175/1520-0442(1993)006<0920:OOSVIA>2.0.CO;2.

Held, I., and B. J. Soden, 2000: Water vapor feedback and global warming. *Annu. Rev. Energy Environ.*, **25**, 441–475, doi:10.1146/annurev.energy.25.1.441.

Henderson, D. S., T. L'Ecuyer, G. Stephens, P. Partain, and M. Sekiguchi, 2013: A multisensor perspective on the radiative impacts of clouds and aerosols. *J. Appl. Meteor. Climatol.*, **52**, 853–871, doi:10.1175/JAMC-D-12-025.1.

Hong, A. C., C. J. Young, M. D. Hurley, T. J. Wallington, and S. A. Mabury, 2013: Perfluorotributylamine: A novel long-lived greenhouse gas. *Geophys. Res. Lett.*, **40**, 6010–6015, doi:10.1002/2013GL058010.

IPCC, 2013: *Climate Change 2013: The Physical Science Basis*. Cambridge University Press, 1535 pp., doi:10.1017/CBO9781107415324.

L'Ecuyer, T. S., N. B. Wood, T. Haladay, G. L. Stephens, and P. W. Stackhouse Jr., 2008: Impact of clouds on atmospheric heating based on the R04 *CloudSat* fluxes and heating rates data set. *J. Geophys. Res.*, **113**, D00A15, doi:10.1029/2008JD009951.

Pierrehumbert, R. T., 1995: Thermostats, radiator fins, and the local runaway greenhouse. *J. Atmos. Sci.*, **52**, 1784–1806, doi:10.1175/1520-0469(1995)052<1784:TRFATL>2.0.CO;2.

Raval, A., and V. Ramanathan, 1989: Observational determination of the greenhouse effect. *Nature*, **342**, 758–761, doi:10.1038/342758a0.

Santer, B. D., and Coauthors, 2007: Identification of human-induced changes in atmospheric moisture content. *Proc. Natl. Acad. Sci. USA*, **104**, 15 248–15 253, doi:10.1073/pnas.0702872104.

Sherwood, S. C., W. Ingram, Y. Tsushima, M. Satoh, M. Roberts, P. L. Vidale, and P. A. O'Gorman, 2010: Relative humidity changes in a warmer climate. *J. Geophys. Res.*, **115**, D09104, doi:10.1029/2009JD012585.

Soden, B. J., and I. M. Held, 2006: An assessment of climate feedbacks in coupled ocean–atmosphere models. *J. Climate*, **19**, 3354–3360, doi:10.1175/JCLI3799.1.

——, D. L. Jackson, V. Ramaswamy, M. D. Schwarzkopf, and X. Huang, 2005: The radiative signature of upper tropospheric moistening. *Science*, **310**, 841–844, doi:10.1126/science.1115602.

Solomon, S., K. H. Rosenlof, R. W. Portmann, J. S. Daniel, S. M. Davis, T. J. Sanford, and G.-K. Plattner, 2010: Contributions of stratospheric water vapor to decadal changes in the rate of global warming. *Science*, **327**, 1219–1223, doi:10.1126/science.1182488.

Stephens, G. L., and T. J. Greenwald, 1991: The Earth's radiation budget and its relation to atmospheric hydrology: 1. Observations of the clear sky greenhouse effect. *J. Geophys. Res.*, **96**, 15 311–15 324, doi:10.1029/91JD00973.

——, and Y. Hu, 2010: Are climate-related changes to the character of global precipitation predictable? *Environ. Res. Lett.*, **5**, 025209, doi:10.1088/1748-9326/5/2/025209.

——, P. M. Gabriel, and P. T. Partain, 2001: Parameterization of atmospheric radiative transfer. Part I: Validity of simple models. *J. Atmos. Sci.*, **58**, 3391–3409, doi:10.1175/1520-0469(2001)058<3391:POARTP>2.0.CO;2.

——, D. O'Brien, P. Pilewskie, S. Kato, and J. Li, 2015: The albedo of Earth. *Rev. Geophys.*, **53**, 141–163, doi:10.1002/2014RG000449.

Taylor, K. E., R. J. Stouffer, and G. A. Meehl, 2012: An overview of CMIP5 and the experiment design. *Bull. Amer. Meteor. Soc.*, **93**, 485–498, doi:10.1175/BAMS-D-11-00094.1.

Teixeira, J., and the AIRS Science Team, 2013: AIRS/Aqua L2 Support Retrieval (AIRS+AMSU) V006. Goddard Earth Sciences Data and Information Services Center, accessed 2 June 2016, doi:10.5067/AQUA/AIRS/DATA207.

Tyndall, J., 1861: On the absorption and radiation of heat by gases and vapours. *Philos. Mag.*, **22**, 169–194, 273–285.

Valero, F. P., W. D. Collins, P. Pilewskie, A. Bucholtz, and P. J. Flatau, 1997: Direct radiometric observations of the water vapor greenhouse effect over the equatorial Pacific Ocean. *Science*, **275**, 1773–1776, doi:10.1126/science.275.5307.1773.

Zelinka, M. D., and D. L. Hartmann, 2012: Climate feedbacks and their implications for poleward energy flux changes in a warming climate. *J. Climate*, **25**, 608–623, doi:10.1175/JCLI-D-11-00096.1.

Zhang, M., and Y. Huang, 2014: Radiative forcing of quadrupling CO_2. *J. Climate*, **27**, 2496–2508, doi:10.1175/JCLI-D-13-00535.1.